IOP Publishing Physica Scripta
Phys. Scr. **T142** (2010) 014064 (6pp) doi:10.1088/0031-8949/2010/T142/014064

# Adaptive wavelet collocation method simulations of Rayleigh–Taylor instability

**S J Reckinger[1], D Livescu[2] and O V Vasilyev[1]**

[1] University of Colorado, Boulder, CO 80309, USA
[2] Los Alamos National Laboratory, Los Alamos, NM 87545, USA

E-mail: scott.reckinger@colorado.edu

Received 25 April 2010
Accepted for publication 2 June 2010
Published 31 December 2010
Online at stacks.iop.org/PhysScr/T142/014064

**Abstract**
Numerical simulations of single-mode, compressible Rayleigh–Taylor instability are performed using the adaptive wavelet collocation method (AWCM), which utilizes wavelets for dynamic grid adaptation. Due to the physics-based adaptivity and direct error control of the method, AWCM is ideal for resolving the wide range of scales present in the development of the instability. The problem is initialized consistent with the solutions from linear stability theory. Non-reflecting boundary conditions are applied to prevent the contamination of the instability growth by pressure waves created at the interface. AWCM is used to perform direct numerical simulations that match the early-time linear growth, the terminal bubble velocity and a reacceleration region.

PACS number: 47.20.Ma

## 1. Introduction

The use of a wavelet-based adaptive method for the simulation of complex fluid systems allows efficient use of computational resources, since high-resolution simulations are performed only where small structures are present in the flow. The wavelets allow the grid to dynamically adapt to the structures in the flow as they evolve in time while maintaining direct control of the error [1]. The adaptive wavelet collocation method (AWCM) is an innovative approach for the numerical simulation of non-equilibrium turbulent processes and has been efficiently used for simulations of incompressible flows [2] and compressible inert and reactive flows [3, 4]. AWCM is yet to be tested for the study of Rayleigh–Taylor instability systems. The extension of AWCM to simulations of Rayleigh–Taylor instability is promising due to the localized nature of the system.

The Rayleigh–Taylor instability, which results when a light fluid pushes on a heavier fluid [5, 6], plays a major role in various systems of interest, including astrophysical [7, 8], atmospherical, inertial confinement fusion [9, 10], etc. When a single-mode, small perturbation is applied to the interface between two fluids, a bubble of lighter fluid penetrates into the heavier fluid. Concurrently, a spike of heavier fluid falls into the lighter fluid. The late-time behavior of the instability in the presence of compressibility and variable density effects is not currently fully understood [11, 12]. However, in order to capture the late-time behavior, the simulations need to be performed in long vertical domains. To minimize the computational effort, high-resolution simulations on such domains could be performed on adaptive grids, where the resolution of the computational grid matches the local scale of the system. Rayleigh–Taylor instability remains a spatially localized phenomenon near the interface well into the turbulent stage. Most of the computational domain is therefore quiescent. The feasibility of applying AWCM to the study of Rayleigh–Taylor instability is tested by simulating the growth of the two-dimensional instability. Of interest for the direct numerical simulations are matching the early time linear growth [13], achieving the terminal bubble velocity [14–16] and observing a reacceleration region [17].

## 2. AWCM

AWCM utilizes wavelets to locally adapt the numerical resolution during the evolution of complex flows [18–20]. Thus, localized structures are well-resolved while optimizing computational resources. In order to simplify the computation of nonlinear terms, a wavelet collocation method is used, which ensures a one-to-one correspondence between grid points and wavelets. Wavelets are functions that are localized in both wave number and physical space, which are used as a set of basis functions to represent the flow in terms of wavelet coefficients. In this sense, wavelets provide both frequency and position information about the

 

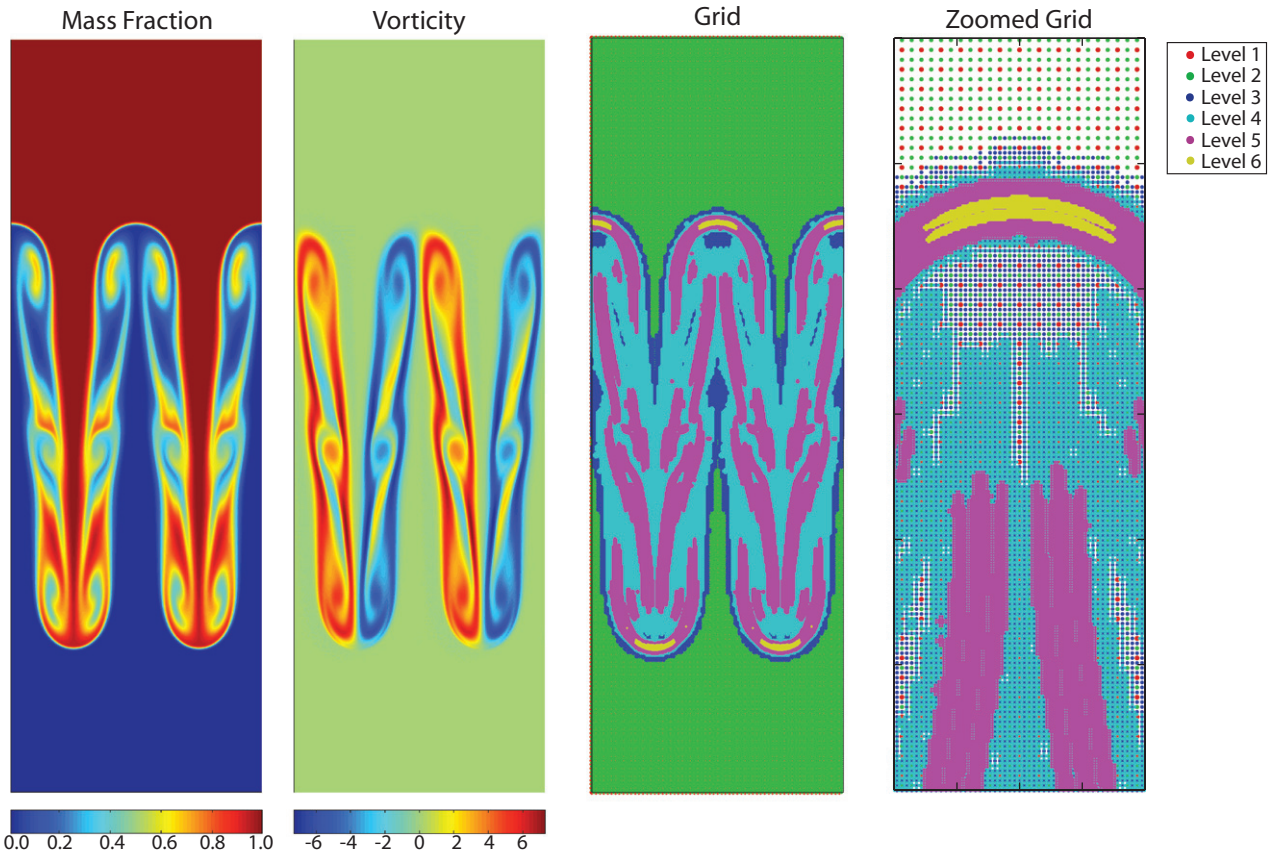


**Figure 1.** Mass fraction, vorticity and the associated adaptive grid for the late-time instability growth.

flow. AWCM uses wavelet decomposition to determine those wavelets that are insignificant for representing the solution while maintaining a direct error control. Once scaling functions, $\phi^j_{\mathbf{k}}(\mathbf{x})$, and wavelet interpolating functions, $\psi^{\mu,j}_{\mathbf{l}}(\mathbf{x})$, are constructed [20], a function $f(\mathbf{x})$ can be decomposed as

$$f(\mathbf{x}) = \sum_{\mathbf{k}} c^0_{\mathbf{k}} \phi^0_{\mathbf{k}}(\mathbf{x}) + \sum_{j=0}^{\infty} \sum_{\mu=1}^{2^n-1} \sum_{\mathbf{l}} d^{\mu,j}_{\mathbf{l}} \psi^{\mu,j}_{\mathbf{l}}(\mathbf{x}). \quad (1)$$

A wavelet coefficient, $d^{\mu,j}_{\mathbf{l}}$, will have a small value unless the function varies on the scale $j$ in the immediate vicinity of the wavelet $\psi^{\mu,j}_{\mathbf{l}}(\mathbf{x})$. For functions where isolated small structures exist on a large-scale background, most of the wavelet coefficients are small. The wavelets associated with coefficients less than a prescribed threshold parameter, $\epsilon$, can be discarded in representing the solution, while retaining an approximation with an error that is $O(\epsilon)$. Derivatives are calculated at the corresponding local resolution using finite differences. Second-generation wavelets are used, which allow the order of the wavelets and thus the order of the finite differences to be easily varied.

When solving evolution problems, such as the growth of Rayleigh–Taylor instability, an adjacent zone is added to the points associated with wavelets, whose coefficients are significant. By adding the nearest neighbors of the significant wavelet coefficients in both position and scale, the computational grid contains points that could become significant during a time step. The dynamic grid adaptation allows efficient use of computational resources for resolving a wide range of scale structures as they evolve. A typical dynamically adapted grid is shown in figure 1 for a late-time Rayleigh–Taylor instability simulation. The effective global resolution is $10\,241 \times 1024$, yet only 3.6% of the points are used (380 166 points, 96.4% compression).

## 3. Model problem

In order to test the applicability of AWCM for direct numerical simulations of the Rayleigh–Taylor instability, a two-dimensional, single-mode system is studied. Linear stability theory offers an early time solution to the instability growth, which is used to test the accuracy of the code.

### *3.1. Governing equations*

Simulations of the two-dimensional, single-mode, miscible Rayleigh–Taylor instability are performed by solving the compressible Navier–Stokes, energy and species mass fraction, $Y_l$, with $l = \overline{1,2}$, transport equations. Along with the ideal gas equation of state, $P = \rho RT$, in dimensional form, the governing equations are [21]

$$\frac{\partial \rho}{\partial t} + \frac{\partial \rho u_j}{\partial x_j} = 0, \quad (2)$$

$$\frac{\partial \rho u_i}{\partial t} + \frac{\partial \rho u_i u_j}{\partial x_j} = -\frac{\partial p}{\partial x_i} - \rho g_i + \frac{\partial \tau_{ij}}{\partial x_j}, \quad (3)$$

$$\frac{\partial \rho e}{\partial t} + \frac{\partial \rho e u_j}{\partial x_j} = -\frac{\partial p u_i}{\partial x_i} - \rho u_i g_i + \frac{\partial \tau_{ij} u_i}{\partial x_j} + \frac{\partial}{\partial x_j}\left(k\frac{\partial T}{\partial x_j}\right) + \frac{\partial}{\partial x_j}\left(D\rho c_{p_l} T \frac{\partial Y_l}{\partial x_j}\right), \quad (4)$$

$$\frac{\partial \rho Y_l}{\partial t} + \frac{\partial \rho Y_l u_j}{\partial x_j} = \frac{\partial}{\partial x_j}\left(D\rho \frac{\partial Y_l}{\partial x_j}\right), \quad (5)$$

where $\rho$ is the density, $P$ is the pressure, $T$ is the temperature, $R$ is the gas constant and $u_i$ is the velocity in the $x_i$-direction and the specific total energy is defined as $e = u_i u_i/2 + c_p T - P/\rho$. The shear stress tensor, assuming Newtonian fluids, is defined as $\tau_{ij} = \mu[\partial u_i/\partial x_j + \partial u_j/\partial x_i - (2/3)(\partial u_k/\partial x_k)\delta_{ij}]$. Fluid properties, such as the dynamic viscosity, $\mu$, heat conduction coefficient, $k$, specific heats at constant pressure and volume, $c_p$ and $c_v$, and mass diffusion coefficient, $D$, are defined as linear combinations of the individual species' properties using the mass fractions. For example, the specific heat at constant pressure is defined as $c_p = c_{p_l} Y_l$, where summation over repeated indices is used.

The system is composed of a heavy fluid lying on top of a lighter fluid in the vertical ($x_1$) direction. The top fluid molar mass is greater than that for the lower fluid, that is, $W_1 > W_2$. Initially, the pressure and temperature at the interface are $P_i$ and $T_i$. The length scale used to non-dimensionalize the equations is the perturbation wavelength, $\lambda$, for the initial interface. The Atwood number, which is a measure of the difference in density of the two fluids, is defined as

$$A = \frac{W_1 - W_2}{W_1 + W_2}. \quad (6)$$

In order to investigate compressibility effects, a distinction is made between fluid compressibility characterized by the values of the ratios of the specific heats, $\gamma_1$ and $\gamma_2$, and compressibility effects in response to the thermodynamic state of the system, characterized by a Mach number defining the size of a characteristic velocity relative to the speed of sound [13]. Since the flow starts with zero velocity, the Mach number is defined based on the gravity wave speed, which characterizes the instability driving force, and the isothermal speed of sound, which removes the effects of the specific heats from the definition [13, 22]. The definition is

$$M = \sqrt{\frac{\bar{\rho} g \lambda}{P_i}}, \quad (7)$$

where $\bar{\rho} = (W_1 + W_2) P_i/(2\mathcal{R} T_i)$, with $\mathcal{R}$ being the universal constant, is the fluid density at the interface, where the two fluids are equally mixed by volume (such that the mole fractions are equal). For certain classes of initial conditions, e.g. thermal equilibrium, $M$ also determines the vertical variations of the equilibrium density and pressure profiles [13, 22]. In these cases, it can be regarded, in addition, as a stratification parameter [11].

### 3.2. Initial conditions

The system is initialized with a hydrostatic background state, to which linear perturbation fields for density and pressure are added. The initial velocity field is zero, representing a system at rest. Plugging $u_i = 0$ into (3), the hydrostatic background state requires that

$$\frac{\partial p^H}{\partial x_1} = -\rho^H g. \quad (8)$$

Assuming a background state in thermodynamic equilibrium, the non-dimensional solution for each fluid is

$$p_m^H = \exp[-M^2(1 \pm A)x_1], \quad (9)$$

$$\rho_m^H = (1 \pm A)\exp[-M^2(1 \pm A)x_1], \quad (10)$$

where the subscript $m = \overline{1,2}$ describes the fluid species. A single-mode perturbation is added to the hydrostatic background state consistent with linear stability theory [13]. The perturbation fields for the two-dimensional system are of the form

$$p_m' = f_m(x_1)\exp(\mathrm{i}kx_2 + nt), \quad (11)$$

$$\rho_m' = \tilde{f}_m(x_1)\exp(\mathrm{i}kx_2 + nt). \quad (12)$$

The $x_1$-dependent functions are solved from the governing equations (2)–(4) with the imposed solution from (11) and (12) [13]. The initial fields for pressure and density for each fluid are then

$$p_m = p_m^H + p_m', \quad (13)$$

$$\rho_m = \rho_m^H + \rho_m'. \quad (14)$$

The initial fields are smoothed at the interface using error functions, $H_\pm(x) = [1 \pm \mathrm{erf}(x/\delta)]/2$, resulting in the full initial pressure and density fields:

$$p = H_+(x_1 + \eta)p_1 + H_-(x_1 + \eta)p_2, \quad (15)$$

$$\rho = H_+(x_1 + \eta)\rho_1 + H_-(x_1 + \eta)\rho_2. \quad (16)$$

The perturbed initial temperature is then determined from the equation of state.

## 4. Numerical implementation

Simulations of the model problem are performed using AWCM. The domain is periodic in the horizontal ($x_2$) direction. The boundary conditions in the vertical ($x_1$) direction are designed to simulate an infinite domain such that any pressure wave approaching the numerical boundaries is not reflected and thus does not interact with and disturb the growth of the instability. Pressure waves are created at the interface at the initial time and travel in the vertical direction. The instability is isolated by applying non-reflecting characteristics-based boundary conditions at the top and bottom of the domain, along with an additional buffer layer of increased viscosity to assist in the damping of the pressure waves.

The non-reflecting characteristics-based boundary conditions are similar to the local one-dimensional inviscid (LODI) conditions introduced by Poinsot and Lele [23]. However, a modification is required for accounting for the hydrostatic background state. The analysis is performed on the one-dimensional Euler equations:

$$\frac{\partial \rho}{\partial t} + \rho\frac{\partial u}{\partial x} + u\frac{\partial \rho}{\partial x} = 0, \quad (17)$$

$$\frac{\partial u}{\partial t} + u\frac{\partial u}{\partial x} + \frac{1}{\rho}\frac{\partial p}{\partial x} = 0, \tag{18}$$

$$\frac{\partial p}{\partial t} + \rho c^2 \frac{\partial u}{\partial x} + u\frac{\partial p}{\partial x} = 0, \tag{19}$$

where $c$ is the speed of sound. The waves are approximately planar, and viscous effects are not considered. Pressure and density can be decomposed into the steady hydrostatic background state and the unsteady fields as follows:

$$p = p^H + \tilde{p}, \tag{20}$$

$$\rho = \rho^H + \tilde{\rho}. \tag{21}$$

The hydrostatic quantities have the relationship given in (8) and are assumed constant with time. However, the hydrostatic fields vary with $x_1$ everywhere, including near the boundaries. Therefore, the hydrostatic background state is removed from the pressure and density evolution terms before the characteristic equations are derived. The modified Euler equations are

$$\frac{\partial \tilde{\rho}}{\partial t} + \rho\frac{\partial u}{\partial x} + u\frac{\partial \tilde{\rho}}{\partial x} = -u\frac{\partial \rho^H}{\partial x}, \tag{22}$$

$$\frac{\partial u}{\partial t} + u\frac{\partial u}{\partial x} + \frac{1}{\rho}\frac{\partial \tilde{p}}{\partial x} = \frac{\rho^H g}{\rho}, \tag{23}$$

$$\frac{\partial \tilde{p}}{\partial t} + \rho c^2 \frac{\partial u}{\partial x} + u\frac{\partial \tilde{p}}{\partial x} = \rho^H g u. \tag{24}$$

The differential characteristic variables for this system are

$$\mathrm{d}v_1 = \rho c\,\mathrm{d}u - \mathrm{d}\tilde{p}, \tag{25}$$

$$\mathrm{d}v_2 = c^2\,\mathrm{d}\tilde{\rho} - \mathrm{d}\tilde{p}, \tag{26}$$

$$\mathrm{d}v_3 = \rho c\,\mathrm{d}u + \mathrm{d}\tilde{p}, \tag{27}$$

which results in the following characteristic equations:

$$\frac{\partial v_1}{\partial t} + (u-c)\frac{\partial v_1}{\partial x} = -(u-c)\rho^H g, \tag{28}$$

$$\frac{\partial v_2}{\partial t} + u\frac{\partial v_2}{\partial x} = u(\gamma - 1)\rho^H g, \tag{29}$$

$$\frac{\partial v_3}{\partial t} + (u+c)\frac{\partial v_3}{\partial x} = (u+c)\rho^H g. \tag{30}$$

Therefore, the LODI conditions are applied only to the unsteady fields, and the hydrostatic background state affects the system through appropriate source terms in the characteristic equations. Incoming characteristics are set to zero for non-reflecting boundary conditions. To ensure a well-posed system consistent with the LODI conditions while considering a viscous flow, the $x_1$ spatial derivatives of the tangential stresses and normal heat flux are set to zero at the boundaries.

In addition to the modified non-reflecting characteristics-based boundary conditions, a buffer layer is added to the domain where the viscosity is slowly increased to partially damp pressure waves approaching the vertical boundaries. Since an adaptive grid is utilized, the computational cost of the buffer layer is negligible. Therefore, the buffer layer can be extended to extreme lengths to accommodate large damping.

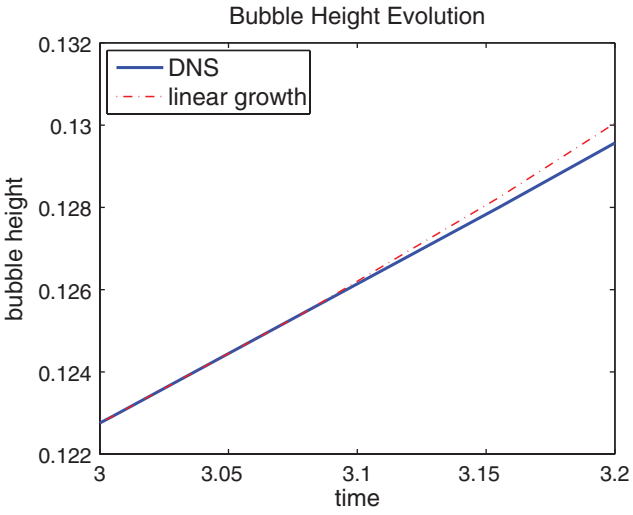


**Figure 2.** Bubble height comparison using linear stability theory for $A = 0.1$ and $M = 0.2$.

## 5. Results

As an initial feasibility check, a simulation is performed in the incompressible limit ($M = 0.2$) and for a small molar mass ratio ($A = 0.1$). The simulation parameters are $Re = 5000$, $\gamma_1 = \gamma_2 = 5/3$, $\delta = 0.02$ and the interface perturbation amplitude $\eta_0 = 0.01$. Late-time plots of the mass fraction, vorticity and grid are shown in figure 1.

The early-time growth of the instability consists of a brief diffusive region where the interface is smoothed slightly, followed by a linear growth regime, as observed in the bubble height evolution presented in figure 2. The linear solution is approximated using

$$n = \left(\frac{gkA}{\psi} + \nu^2 k^4\right)^{1/2} - (\nu + D)k^2, \tag{31}$$

where diffusive and viscous effects are considered [24]. This formula yields similar results to those obtained numerically in [11]. For the values considered here, diffusive and viscous effects on the linear growth rate account for a 30% decrease from the incompressible, immiscible result, $n = \sqrt{gkA}$. Compressibility has a less than 2% influence on the linear growth rate.

As the flow departs the linear stability theory regime, the region near the tip of the bubble can be described using potential flow theory for some time, before significant vortical motions are generated. During this potential flow stage, a terminal bubble velocity has been derived for the incompressible case [25]. The non-dimensional terminal bubble velocity is

$$v_\mathrm{b}^* = \frac{v_\mathrm{b}}{\sqrt{g\lambda}} = \sqrt{\frac{1}{C_\mathrm{d}}\frac{2A}{(1+A)}}, \tag{32}$$

where the coefficient is $C_\mathrm{d} = 6\pi$, for a two-dimensional system. Once the bubble reaches the terminal velocity,

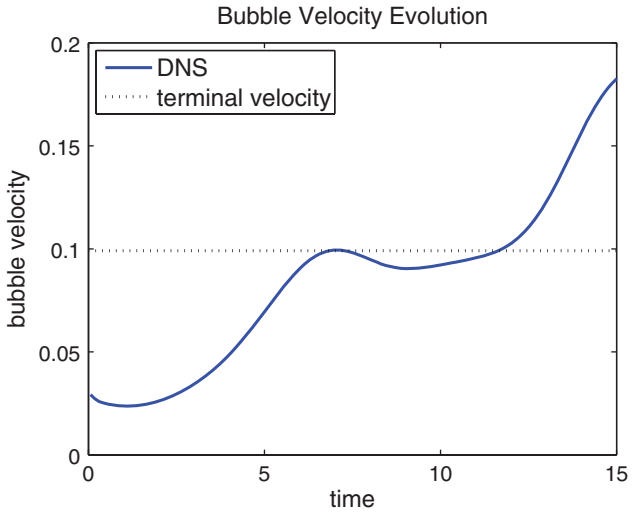


**Figure 3.** Bubble velocity for $A = 0.1$ and $M = 0.2$. The dotted line in the bubble velocity plot represents the analytic terminal bubble velocity, $v_b^*$.

a brief deceleration is observed, followed by a reacceleration region [17]. The wavelet-based simulation of the small Atwood, quasi-incompressible Rayleigh–Taylor instability matches this behavior, as shown in figure 3.

To ensure that the simulations are converged, a resolution study is presented in figure 4. By decreasing the wavelet coefficient threshold parameter $\epsilon$, the effective local resolution is increased since more points are kept on the adaptive grid. The zoomed view of the curves for the bubble height show the results converging for smaller values of $\epsilon$.

## 6. Conclusions

The physics-based mesh adaptivity offered by AWCM makes it an innovative approach for studying the fundamental aspects of non-equilibrium turbulent processes, specifically in cases where fluid mixing and turbulent intermittency occur in localized regions of the system. As a proof of concept, AWCM is applied for the simulation of a two-dimensional Rayleigh–Taylor instability. The use of AWCM for direct numerical simulations of Rayleigh–Taylor systems is promising, since the spatial localization of the mixing layer leads to significant compression in the number of points necessary, while maintaining a high effective resolution. Wave motion in the compressible case is efficiently captured by the AWCM, since the mesh dynamically adapts to the solution during wave propagation. Unlike adaptive mesh refinement techniques, AWCM offers an explicit error control through the threshold parameter $\epsilon$. The use of AWCM allows for the addition of a long buffer layer for the damping of waves created at the interface. Non-reflecting boundary conditions are applied at the top and bottom of the domain to further isolate the instability.

Numerical tests show that the method successfully captures the linear regime, bubble and spike formations and late-time flow characteristics for the single-mode perturbation case. Simulations at higher Atwood and Mach numbers for observing the variable density and compressibility effects on the late-time development of Rayleigh–Taylor instability are under way and these will be published elsewhere.

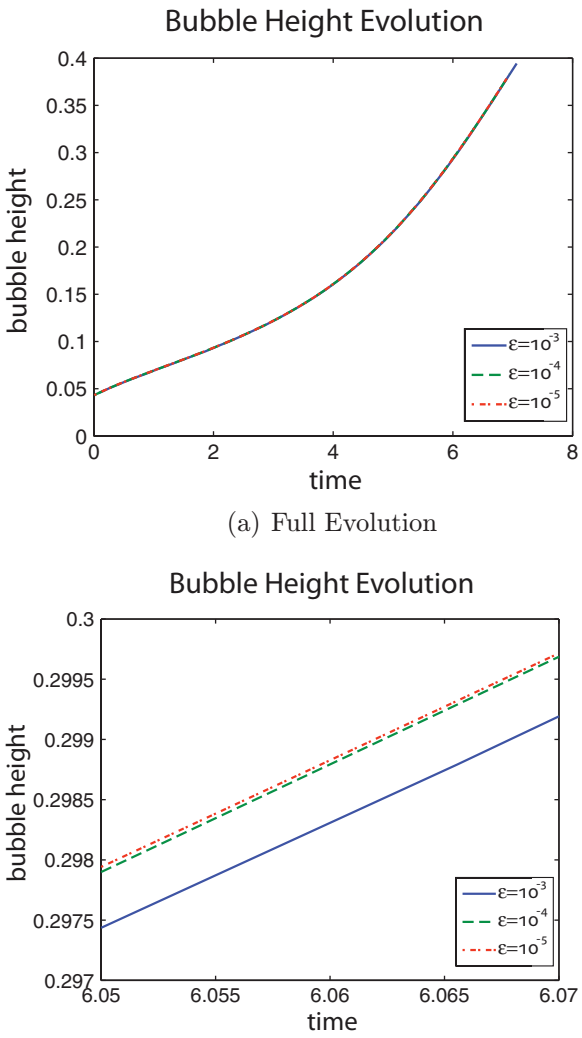


(a) Full Evolution

(b) Zoomed View

**Figure 4.** Bubble height evolution for different values of the wavelet coefficient threshold $\epsilon$, which varies the effective resolution. A zoomed view is shown for visualization of the various curves.

## Acknowledgments

The Los Alamos National Laboratory is operated by Los Alamos National Security, LLC, for the US Department of Energy's NNSA under contract number DE-AC52-06NA25396. This paper and part of the study described herein were made possible by funding from the LDRD program at Los Alamos National Laboratory through project numbers 20090058DR and 20070195ER. Computational resources were provided by LANL Institutional Computing (IC) Program.

## References

[1] Schneider K and Vasilyev O V 2010 Wavelet methods in computational fluid dynamics *Annu. Rev. Fluid Mech.* **42** 473–503

[2] Kevlahan N K R and Vasilyev O V 2005 An adaptive wavelet collocation method for fluid–structure interaction at high Reynolds numbers *SIAM J. Sci. Comput.* **26** 1894–915

[3] Liu Q and Vasilyev O V 2007 A Brinkman penalization method for compressible flows in complex geometries *J. Comput. Phys.* **227** 946–66

[4] Regele J D and Vasilyev O V 2009 An adaptive wavelet-collocation method for shock computations *Int. J. Comput. Fluid Dyn.* **23** 503–18
[5] Taylor G 1950 The instability of liquid surfaces when accelerated in a direction perpendicular to their planes. I *Proc. R. Soc.* A **201** 192–6
[6] Chandrasekhar S 1981 *Hydrodynamic and Hydromagnetic Stability* (New York: Dover) pp 428–77
[7] Remington B A, Weber S V, Marinak M M, Haan S W, Kilkenny J D, Wallace R J and Dimonte G 1995 Single-mode and multi-mode Rayleigh–Taylor experiments on Nova *Phys. Plasmas* **2** 241–55
[8] Farley D R and Logory L M 2000 Single-mode, nonlinear mix experiments at high Mach number using Nova *ApJS* **127** 311–6
[9] Kilkenny J D, Glendinning S G, Haan S W, Hammel B A, Lindl J D, Munro D, Remington B A, Weber S V, Knauer J P and Verdon C P 1994 A review of the ablative stabilization of the Rayleigh–Taylor instability in regimes relevant to inertial confinement fusion *Phys. Plasmas* **1** 1379–89
[10] Knauer J P *et al* 2000 Single-mode, Rayleigh–Taylor growth-rate measurements on the OMEGA laser system *Phys. Plasmas* **7** 338–45
[11] Gauthier S and Le Creurer B 2010 Compressibility effects in Rayleigh–Taylor instability-induced flows *Phil. Trans. R. Soc.* A **368** 1681–704
[12] Livescu D, Ristorcelli J R, Gore R A, Dean S H, Cabot W H and Cook A W 2009 High-Reynolds number Rayleigh–Taylor turbulence *J. Turbul.* **10** 1–32
[13] Livescu D 2004 Compressibility effects on the Rayleigh–Taylor instability growth between immiscible fluids *Phys. Fluids* **16** 118–27
[14] Goncharov V N 2002 Analytical model of nonlinear, single-mode, classical Rayleigh–Taylor instability at arbitrary Atwood numbers *Phys. Rev. Lett.* **88** 134502
[15] Waddell J T, Niederhaus C E and Jacobs J W 2001 Experimental study of Rayleigh–Taylor instability: low Atwood number liquid systems with single-mode initial perturbations *Phys. Fluids* **13** 1263–73
[16] Ramaprabhu P and Dimonte G 2005 Single-mode dynamics of the Rayleigh–Taylor instability at any density ratio *Phys. Rev.* E **71** 036314
[17] Ramaprabhu P, Dimonte G, Young Y N, Calder A C and Fryxell B 2006 Limits of the potential flow approach to the single-mode Rayleigh–Taylor problem *Phys. Rev.* E **74** 066308
[18] Vasilyev O V and Paolucci S 1997 A fast adaptive wavelet collocation algorithm for multidimensional PDEs *J. Comput. Phys.* **138** 16–56
[19] Vasilyev O V and Bowman C 2000 Second-generation wavelet collocation method for the solution of partial differential equations *J. Comput. Phys.* **165** 660–93
[20] Vasilyev O V 2003 Solving multi-dimensional evolution problems with localized structures using second generation wavelets *Int. J. Comput. Fluid Dyn.* **17** 151–68
[21] Williams F A 1985 *Combustion Theory* (Menlo Park, CA: Benjamin/Cummings) pp 2–4
[22] Yu H and Livescu D 2008 Rayleigh–Taylor instability in cylindrical geometry with compressible fluids *Phys. Fluids* **20** 104103
[23] Poinsot T J and Lele S K 1992 Boundary-conditions for direct simulations of compressible viscous flows *J. Comput. Phys.* **101** 104–29
[24] Duff R E, Harlow F H and Hirt C W 1962 Effects of diffusion on interface instability between gases *Phys. Fluids* **5** 417–25
[25] Oron D, Arazi L, Kartoon D, Rikanati A, Alon U and Shvarts D 2001 Dimensionality dependence of the Rayleigh–Taylor and Richtmyer–Meshkov instability late-time scaling laws *Phys. Plasmas* **8** 2883–9